One-Way 3D Printed Shape Memory Polymers

A Major Qualifying Project
Submitted to the Faculty of
Worcester Polytechnic Institute
in partial fulfillment of the requirement for the
Degree in Bachelor of Science
in
Mechanical and Chemical Engineering
By

Connor Barrett

Joseph Presing

Date: 04/25/2017
Project Advisors:

Professor Amy M. Peterson

Anthony D'Amico

Abstract

The goal of this project was to better understand the residual stresses imparted into 3D printed polymer parts and then to be able to predict irreversible thermal strain from annealing. Residual stresses in 3D printed pieces are, in part, controlled by raster angle and layer thickness; the two print parameters examined in this project. Through fitting Hooke's Law of Plane and Shear Stress to our experimental data, equations representing the magnitude and direction of irreversible thermal strain and shear strain were formed. These equations were used in the creation of an algorithm that allowed an input of desired final dimensions and output the necessary print parameters to achieve them. This project added a new dimension to the additive manufacturing field by allowing for the creation of 3D printed one-way shape memory polymers. While the strength of pieces was not maximized, the project created a multifunctionality that previously did not exist.

Acknowledgements

We would like to thank our advisors Professor Amy M. Peterson and Anthony D’Amico for their continued support and guidance throughout the completion of this project. We would also like to thank Worcester Polytechnic Institute for providing us the opportunity and space to complete this project.

Executive Summary

Additive manufacturing (AM) is the process of creating a 3–dimensional object through the addition of material [1]. Fused deposition modeling (FDM) is a common method of polymer AM in which an extruder deposits roads of polymer filament onto a surface [2]. This process is repeated, layer by layer, until the print is completed. During the FDM process, mismatches in the coefficients of thermal expansion (CTE) arise when the molten polymer layer is placed on the previous glassy polymer layer [3]. The mismatch in CTE can lead to a build-up of residual stress within the FDM part, which has been shown to affect the magnitude of irreversible thermal strain from annealing [3]. To the authors' knowledge, the relationship between the magnitude and direction of irreversible thermal strain in polymer AM and residual stress has not been previously studied.

The buildup of residual stress is, in part, dictated by the layer thickness and the raster angle of the print [3,4]. Both raster angle and layer thickness are parameters that can be easily modified in FDM. This research project was a parametric study to gain a more robust understanding of the relationships between raster angle, layer thickness, and irreversible thermal strain based on first principles. To accomplish this goal, the following aims were completed.

Aim 1: Determine the relationships between raster angle, layer thickness, and the direction of irreversible thermal strain

Aim 2: Develop an algorithm that relates layer thickness and raster angle to the direction and magnitude of irreversible thermal strain.

Aim 3: Validate and refine the algorithm by attempting to achieve desired irreversible thermal deformations.

Aim 4: Create multiple designs containing different combinations of layer thicknesses and raster angles to achieve the same post-annealed final shape.

The completion of the algorithm and the validation via the design concept will provide a new tool for the AM process. A strong relationship between the raster angle, layer thickness, and irreversible thermal strain was determined. Experimental relations were consistent with predictions from the algorithm derived from the application of Hooke's law on a material undergoing 3D stress. The algorithm serves as a tool to create FDM printed parts that will anneal into a desired shape. Although the full scope of each controllable print parameter and their effect on residual stress is unknown, it does provide an opening into a new field of AM. By adding the ability to predict the post-annealed structure, 3D printed pieces can be used for more direct roles with a lower chance of failure. Therefore, this research helps move 3D printing away from the realm of simply prototyping. If

Table of Contents

Abstract 2

Acknowledgements 3

Executive Summary 4

1. Introduction 7

2. Materials and Methods 11

  - 2.1 Additive manufacturing of samples: 11
  - 2.2 Thermal expansion testing: 11
  - 2.3 Measuring Protocol 12
  - 2.4 Creation of Algorithm: 13
  - 2.5 Validation and Refinement of Algorithm: 16

3. Results 17

  - 3.1 Heat Transfer in Annealing Process 17
  - 3.2 Effect of Gravity on Anneal Process 17
  - 3.3 Print Parameters 18
  - 3.4 Determine Optimal Annealing Time: 19
  - 3.5 Effect of Layer Thickness 21
  - 3.6 Overall Effect of Raster Angle 22
  - 3.7 Discussion of Algorithm 24
  - 3.8 Proof of Concept 28

4. Conclusion 31

References 32

List of Figures

Figure 1: A) Various infill percentage [6]. B) Raster angle is shown [7] 7

Figure 2: Various numbers of shells in a print [9] 8

Figure 3: A two-way shape memory cycle [17] 9

Figure 4: How samples were labeled 11

Figure 5: Angle of sample measured 12

Figure 6: A) Shows X-axis measurements. B) Shows the Y-axis measurements 12

Figure 7: A) Shows small lips resulting from the printing process. B) Shows lips after the annealing process 13

Figure 8: The post-anneal x and y measurements taken 13

Figure 9: Representation of FΘ,x and FΘ,y 14

Figure 10: A sample annealed without a firebrick (left) and with a firebrick (right) 17

Figure 11: Gravity vs. Control Samples 18

Figure 12: On the left, 70% infill. On the right, 80% infill 19

Figure 13: On the left, 90% infill and 100% infill on the right 19

Figure 14: X-axis Strain vs. Anneal Time 20

Figure 15: Y-axis Strain vs. Anneal Time 20

Figure 16: Z-axis Strain vs. Anneal Time 21

Figure 17: Average Strain vs. layer thickness for 0° degree raster in the X and Z-axis 21

Figure 18: Average X-axis strain vs. raster angle 22

Figure 19: Average X-axis strain vs. raster angle 23

Figure 20: Average Z-axis strain vs. raster angle 23

Figure 21: Shear strain vs. raster angle at various layer thicknesses 24

Figure 22: Calculated X-axis Strain vs. Measured Strain at 100µm-400µm 25

Figure 23: Calculated Y-axis Strain vs. Measured Strain at 100µm-400µm 26

Figure 24: Calculated Z-axis Strain vs. Measured Strain at 100µm-400µm 27

Figure 25: Calculated Shear Strain vs. Measured Shear Strain at 100µm-400µm 28

Figure 26: Percent Error vs. Type of Strain for all designs 29

Figure 27: Shear Strain Deviation 30

1. Introduction

Additive manufacturing is the process of creating an object through addition of material. Rather than machining a block of raw material into the desired shape, AM techniques build from the ground up, often layer by layer [1]. Over the past several decades, different AM processes have emerged. Each utilizes different techniques to fuse material. Examples include the use of lasers (selective laser sintering), UV light curing (stereolithography), and FDM [2,5]. This research focused on developing new FDM techniques.

The FDM process starts in a design program where users create their idea. Users then export the file as an .STL to a slicing software that divides the piece into layers. A variety of parameters such as infill percentage, raster angle, and layer thickness can be set in the slicing software to define how each layer is printed. Infill percentage, as shown in Figure 1A, is the amount of material used inside the piece. Raster angle, as shown in Figure 1B, is the orientation of straight beads of filament have with respect to the front of the build plate. Layer thickness, also shown in Figure 1B, is the height of each layer. A smaller layer thickness results in a smoother print but also increases the print time.

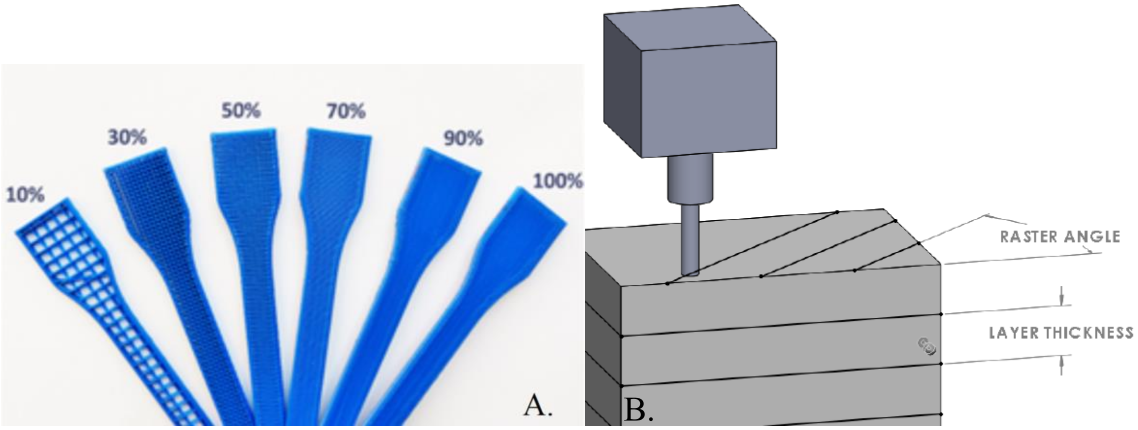

Figure 1: A) Various infill percentage [6]. B) Raster angle is shown [7]

Raster angle is often hidden by the outline shell of each layer. Pieces can be printed with one or more shells depending on the user preference, as seen in Figure 2. While printing with no shells is possible, these pieces lack the set outline shape and often do not print as intended. The extrusion temperature is set based on the material printed, with acrylonitrile butadiene styrene (ABS) typically printed at 230°C [8]. Each parameter affects the properties of the sample and this research examines the effect layer thickness and raster angle have on the buildup of residual stresses.

Figure 2: Various numbers of shells in a print [9]

Residual stresses can compromise the properties of FDM printed polymers. It has been observed in previous studies that residual stresses can negatively impact the printing process by causing cracking, size imperfections, and possibly fabrication failure [10]. Residual stresses arise in FDM printed parts due to mismatches in the CTEs, which are caused by the molten polymer layer being placed on the previous glassy polymer layer [3]. The rapid cooling of polymers in AM also contributes to these mismatches in CTE. Therefore, the buildup of stresses is uniquely large in AM. Thus, certain methods are used to minimize the initial stress buildup as well as relax them after printing.

Heating a polymer above the glass transition temperature (T_g) allows for enough mobility to relieve the residual stress through irreversible thermal strain [4]. The magnitude of the resulting irreversible thermal strain is related to the amount of residual stress relieved [4]. In other manufacturing methods, such as injection molding, the polymer cools less rapidly and more evenly allowing for the relaxation of more stress while above T_g. Therefore, while annealing 3D printed parts, there is often greater stress relieved causing greater amounts of strain.

Both raster angle and layer thickness play a role in how these residual stresses develop [3,4,11]. D'Amico et al. demonstrated that, as layer thickness is decreased, irreversible thermal strain due to residual thermal stress increases [3]. The stresses have also been predicted to form in the direction of the extruded roads [3]. Using these two concepts, the stress and resulting strain could be controlled giving the pieces a new multifunctionality. Rather than attempting to reduce the deformation from annealing, it could be controlled to create pieces that could be considered one-way shape memory polymers.

Shape memory polymers (SMPs) are a class of smart materials that react to various stimuli and return to a predetermined shape. Smart material defines a material that changes properties with specific stimuli. SMPs can be bent, stretched, and twisted but return to their original shape when exposed to the proper conditions. Stimuli of SMPs vary greatly with thermal stimulation being the most common [12]. These polymers have a wide range of applications from aerospace to biomedical due to their unique properties [13].

The first shape memory polymer was reported in 1984 by CdF-Chimie Company of France. Norbornene-based polymers were later commercialized by Nippon Zeon Company of Japan. Early SMPs had limited processibility. However, later advances by Nagoya Research and Development Center of Mitsubishi Heavy Industry resulted in more favorable processibility and mechanical properties [14]. These polyurethane-based SMPs had more favorable properties due to a greater control over the structure. Specifically, polyurethane SMPs can be created with a wide range of T_g which diversifies the possible applications [15].

The shape memory properties of the polymers are due to a change in the Young's modulus after a certain phase transition temperature [15]. This transition temperature can be T_g or the melting point of the polymer. Young's modulus, also known as elastic modulus, defines the relationship between the tensile stress and the tensile strain of a material [16]. When the SMP is heated beyond the transition temperature, stress can be applied to introduce strain within the polymer. If the strain is maintained while the polymer cools below the transition temperature, the stress is trapped within the polymer. The stress can be released by heating the SMP back above the transition temperature allowing the polymer to return to its original shape [15]. This shape change cycle can be seen in Figure 3.

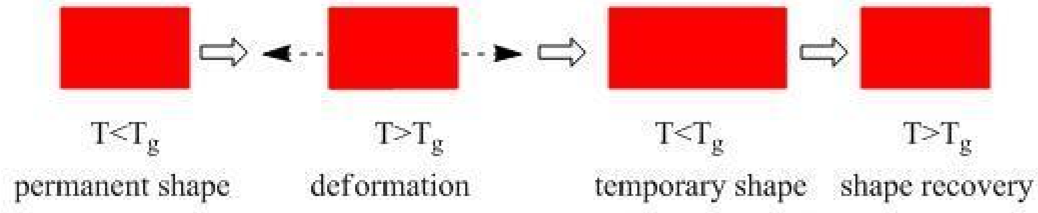

Figure 3: A two-way shape memory cycle [17]

SMPs have a wide range of applications today. They are desirable in aerospace applications because they are lower weight than similar mechanical solutions [13]. The textile industry has begun using the polymers to create smarter clothing that becomes more breathable with increased temperature [15]. SMPs have also been used as orthodontic wires because of the ease of processing and good appearance. Further medical applications of SMPs include expandable stents, artificial muscles, and needle designs [12].

Some applications for SMPs call for two-way SMPs while others only need the initial shape change seen in one-way SMPs. Two-way SMPs are able to deform to a different shape and then return to the original shape. One-way SMPs deform to a certain shape upon stimulus but cannot return to the original shape [12]. An advantage of one-way SMPs is that the shape memory is preprogrammed during manufacturing. Self-deploying solar sails and antenna could make use of one-way SMPs because the initial shape does not need to be recovered [13]. 3D printed SMPs explored in this research have their shape memory programmed into the pieces in the form or the residual stresses. These types of 3D printed one-way SMPs are easy to create and are becoming increasingly available with the rapidly expanding AM industry.

Residual stresses have typically been seen as a detriment in the 3D printing process [10]. The 3D printed products of today are widely designed to not be heated beyond the T_g of the material after the print. With uncontrolled residual stresses, the deformation seen through annealing printed samples is also uncontrolled. The object of this research was to utilize print parameters to predict deformation using an algorithm.

To create the algorithm, experimental data was fit to first principles of applied stress and resulting strain. A desired magnitude of deformation and shear strain is input into the algorithm which then outputs the appropriate layer thickness and raster angle to achieve that deformation. Such an algorithm is desirable because it allows for easily created one-way SMPs. Layer thickness and raster angle can easily be changed to create samples with different stress buildup. This algorithm helps with the understanding of how 3D printers function and how each parameter can affect the resulting properties. A greater degree of control over printed sample properties expands the possible applications of 3D printers. Since this research focused on the deformation, the results can also be used to minimize deformation. Therefore, the algorithm adds the flexibility to decide whether or not to have the one way shape memory effects within a print.

Results from this project only encompass two parameters of the printing process. The parameters are easy to modify which facilitates testing a wide range of combinations and creates data that is easily analyzed. However, other parameters of possibly equal influence and importance have not yet been completely researched such as the effect of print speed, outline shells, and changes in raster width. With these limitations, the results of researching only the raster angle and layer thickness are still robust in that the results do follow theoretical trends, suggesting that the major influences on strain were assessed. This research sought to demonstrate that direction and amount of deformation from annealing could be predicted given the layer thickness and raster angle.

2. Materials and Methods

2.1 Additive manufacturing of samples:

Samples were prepared using a MakerBot Replicator 2X, a commercially available FDM printer from MakerBot Industries. The samples were produced from MakerBot brand, natural colored ABS filament. To minimize temperature fluctuations, the FDM printer resided in a fume hood. Samples were produced with dimensions of 15mm x 10mm x 30mm (X, Y, Z). The raster angle was determined from the X-axis of the printed part as seen in Figure 1b.

Samples were printed at an extrusion temperature of 230°C and a build plate temperature of 115°C. 100% infill was used and the extrusion width (width used for the slicing software) was set to 0.45mm, which was the measured width of extruded filament. Six samples were prepared in a single print. After samples were printed, they were labeled with their corresponding raster angle and layer thickness on the XZ plane (Figure 4). Samples were allowed to cool for one day before being measured using the measuring protocol described in section 2.3.

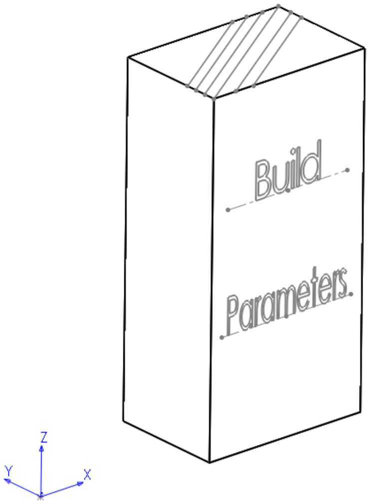

Figure 4: How samples were labeled

2.2 Thermal expansion testing:

To determine the magnitude of the irreversible thermal strain, samples were placed into an oven that was set to a temperature above the T_g of ABS. The T_g of ABS filament was determined to be 115.7°C based on the peak in tan δ in Dynamic Mechanical Analysis performed at 1 Hz, although Differential Scanning Calorimetry provides a lower T_g value of about 105°C [3,18]. 120°C was selected for the annealing temperature. A higher temperature was not used to both avoid thermal degradation of the ABS as well as concerns that ABS would flow under these conditions. Previous research suggests that ABS fully degrades at temperatures between 380°C and 500°C and that some mass is lost at temperatures below that range [19]. Three samples of each raster angle and layer thickness combination were printed. In each print, samples of two different raster angles were printed left to right on the build plate totaling six samples per print. After the samples cooled, they were marked as shown in Figure 4. Samples were annealed in the oven at

120°C for t_{anneal} of 48 hours. The oven used was a VWR small utility oven with a volume of one cubic foot. Samples were annealed on firebricks to reduce warping caused by uneven heating from the oven bed. Firebricks were preheated in the oven prior to annealing the samples. Samples were placed on the firebricks with the XZ plane parallel to the oven base to maintain consistent annealing protocol. Additionally, samples of same raster angle and layer thickness were placed far away from each other to minimize the influence of spatial variations in temperature. After the annealing process was complete, samples were removed from the over and were allowed to equilibrate at room temperature for one day. Samples were then measured again and another photo was taken to determine the shear strain. Figure 5 shows the angle that was measure with respect to the labeled face. Note that the angle measured ϕ, is the complementary angle to the shear strain.

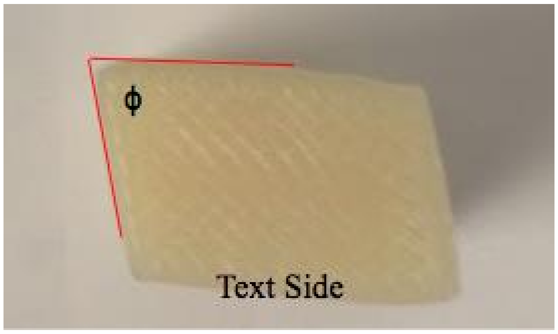

Figure 5: Angle of sample measured

2.3 Measuring Protocol

Each sample was measured at three points in each axis before and after the annealing process. The measurements taken were X-bottom, X-mid, X-top, Y-bottom, Y-mid, Y-top, Z-front, Z-mid, and Z-back. Three points of measurement were taken in each axis to account for error in the printing process. The bottom measurement was the face of the sample that was in contact with the build plate during the printing process. For all measurements, a set of digital calipers with 0.01mm accuracy was used. For the X-axis and Y-axis measurements, the bottom measurement was taken at the base of the sample, the mid measurement was approximately the middle of the Z-axis, and the top measurement was taken at the top (Figure 6).

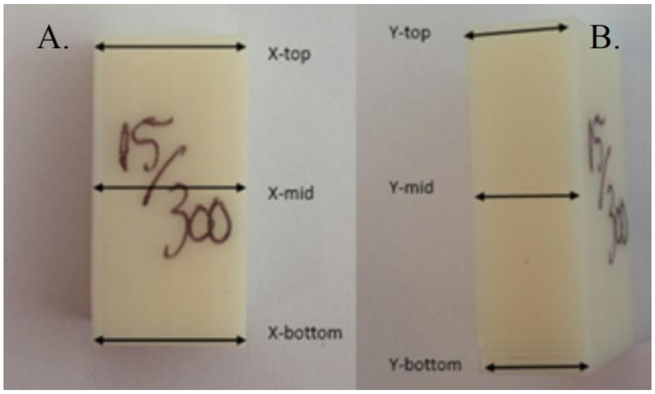

Figure 6: A) Shows X-axis measurements. B) Shows the Y-axis measurements

Some of the bottom and top edges of the part had a slight lip due to the difficulty in printing corners because the filament is extruded with a circular cross section. This lip was avoided in the measuring of the samples (Figure 7A). Similarly, after annealing, the lip in samples was avoided (Figure 7B).

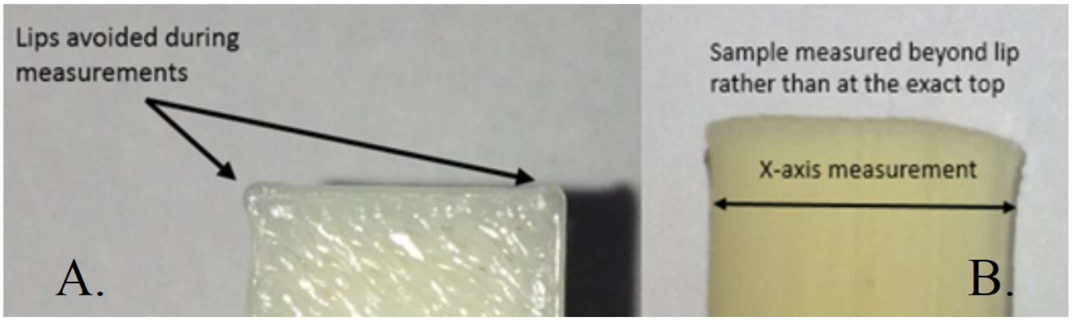

Figure 7: A) Shows small lips resulting from the printing process. B) Shows lips after the annealing process

Therefore, the bottom measurements were not always taken at the exact base of the samples but rather a short distance (~1-3mm) from the base. The annealed samples were measured with the calipers parallel to the sides of the sample (Figure 8).

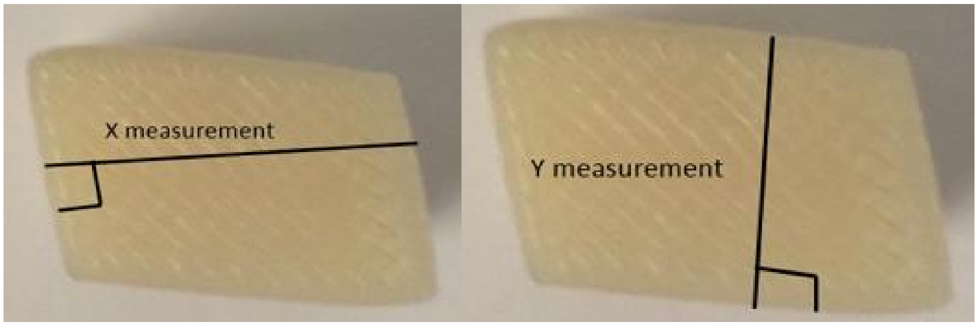

Figure 8: The post-anneal x and y measurements taken

2.4 Creation of Algorithm:

To create the algorithm relating raster angle, layer thickness and irreversible thermal strain, the algorithm was broken down into 4 components, X-axis, Y-axis, Z-axis, and shear strain. The application of Hooke's Law on a material undergoing three dimensional stress (triaxial loading) in a homogenous and isotropic system was used as a model for this relationship. These initial equations modeling the X-axis, Y-axis, Z-axis, and shear strain respectively, are shown below (Equations 1-4).

$$\varepsilon_x = \frac{1}{E} * [\sigma_x - v_{xy}(\sigma_y + \sigma_z)] \qquad \textbf{\textit{(Eq. 1)}}$$

$$\varepsilon_y = \frac{1}{E} * [\sigma_y - v_{xy}(\sigma_z + \sigma_x)] \qquad \textbf{\textit{(Eq. 2)}}$$

$$\varepsilon_z = \frac{1}{E} * [\sigma_z - v_z(\sigma_x + \sigma_y)] \qquad \textbf{\textit{(Eq. 3)}}$$

$$\gamma_{xy} = \frac{\tau_{xy}}{G} \qquad \textbf{\textit{(Eq. 4)}}$$

The variables, E, σ_x, σ_y, σ_z, τ_{xy} ,and G represent the elastic modulus of ABS at 25° C, the normal stress in the X-axis, the normal stress in the Y-axis, the normal stress in the Z-axis, the shear stress in the XY-plane, and the shear modulus, respectively. Additionally, v_{xy} represented the Poisson's ratio in the X and Y-axis. v_z was the Poisson ratio derived from the application of Hooke's law for a material undergoing 3-dimensional stress. v_z was considered different from v_{xy} due to the anisotropic nature of 3D printed parts. Equations 1-4 were solved assuming the stress in the Z-axis direction was negligible ($\sigma_z = 0$), giving Equations 5-7.

$$\varepsilon_x = \frac{1}{E} * [\sigma_x - v_{xy}(\sigma_y)] \qquad \textbf{\textit{(Eq. 5)}}$$

$$\varepsilon_y = \frac{1}{E} * [\sigma_y - v_{xy}(\sigma_x)] \qquad \textbf{\textit{(Eq. 6)}}$$

$$\varepsilon_z = \frac{1}{E} * [-v_z(\sigma_x + \sigma_y)] \qquad \textbf{\textit{(Eq. 7)}}$$

To determine σ_x, σ_y, and τ_{xy} the normal and shear forces acting on XZ and YZ-planes needed to be determined. It was hypothesized that a constant force, $F_{r,}$ was acting parallel to each road. The net force acting in the X-axis ($F_{\Theta,x}$) was different then the net force acting in the Y-axis ($F_{\Theta,y}$) due to a different number of roads along the sample's length and width. This can be seen in Figure 9. Θ is the raster angle of the given sample.

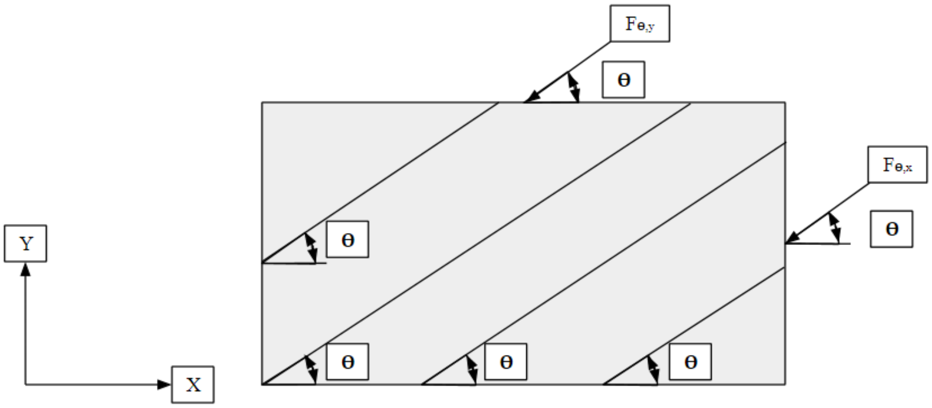

Figure 9: Representation of FΘ,x and FΘ,y

$F_{\Theta,x}$ and $F_{\Theta,y}$ can be determined using the number of roads along the X-axis of the part n_x, the number of roads along the Y-axis of the part n_y, and the number of roads along the Z-axis of the part n_z. The equations for n_x, n_y, n_z, $F_{\Theta,x}$, and $F_{\Theta,y}$ are given by Equations 8-12.

$$n_x = \frac{L_x * sin(\Theta)}{w_r} \qquad \textbf{\textit{(Eq. 8)}}$$

$$n_y = \frac{L_y * cos(\Theta)}{w_r} \qquad \textbf{\textit{(Eq. 9)}}$$

$$n_z = \frac{L_z}{l_t} \qquad \textbf{\textit{(Eq. 10)}}$$

$$F_{\Theta,x} = n_y * n_z * F_r \qquad \textbf{\textit{(Eq. 11)}}$$

$$F_{\Theta,y} = n_x * n_z * F_r \qquad \textbf{\textit{(Eq. 12)}}$$

In Equations 8-12 $w_r$is the extrusion width of the samples, $L_x$is the initial length of the sample in the X-axis direction, L_y is the initial length of the sample in the Y-axis direction, $L_z$is the initial length of the samples in the Z-axis direction, and l_t is the layer thickness of the sample. $F_{\Theta,x}$ and $F_{\Theta,y}$ can then be broken down into their respective shear $(F_{s,x}, F_{s,y})$ and normal force $(F_{n,x}, F_{n,y})$ components given by Equations 13-16.

$$F_{s,x} = F_{\Theta,x} * sin(\Theta) \qquad \textbf{\textit{(Eq. 13)}}$$

$$F_{s,y} = F_{\Theta,y} * cos(\Theta) \qquad \textbf{\textit{(Eq. 14)}}$$

$$F_{n,x} = F_{\Theta,x} * cos(\Theta) \qquad \textbf{\textit{(Eq. 15)}}$$

$$F_{n,y} = F_{\Theta,y} * sin(\Theta) \qquad \textbf{\textit{(Eq. 16)}}$$

Using the shear and normal forces in Equations 13-16, σ_x, σ_y, and τ_{xy} can be written as Equations 17-19 as shown below.

$$\tau_{xy} = \frac{F_{s,y}}{L_x * L_z} = \frac{F_{s,x}}{L_y * L_z} = \frac{\sin(\Theta) * \cos(\Theta) * F_r}{w_r * l_t} \qquad \textbf{\textit{(Eq. 17)}}$$

$$\sigma_x = \frac{F_{n,x}}{L_y * L_x} \qquad \textbf{\textit{(Eq. 18)}}$$

$$\sigma_y = \frac{F_{n,y}}{L_x * L_z} \qquad \textbf{\textit{(Eq. 19)}}$$

Using Equations 5-19, ε_x, ε_y, ε_z, and γ_{xy} can then be written as Equations 20-24.

$$\varepsilon_x = \frac{F_r}{E * w_r * l_t} * (cos^2(\Theta) - v_{xy} sin^2(\Theta)) \qquad \textbf{\textit{(Eq. 20)}}$$

$$\varepsilon_y = \frac{F_r}{E * w_r * l_t} * (sin^2(\Theta) - v_{xy} cos^2(\Theta)) \qquad \textbf{\textit{(Eq. 21)}}$$

$$\varepsilon_z = \frac{F_r}{E * w_r * l_t} * (-v_z) \qquad \textbf{\textit{(Eq. 22)}}$$

$$\gamma_{xy} = \frac{F_r}{E * w_r * l_t} * sin(\Theta) * cos(\Theta) * 2\left(1 + v_{xy}\right) \qquad \textbf{\textit{(Eq. 23)}}$$

Notice the arising stress term, $\frac{F_r}{E * w_r * l_t}$ which represent the stress in each road. The emergence of this term further suggests that the approach to the derivation was appropriate. Further details discussing the fit of these equations can be found in the Results section.

2.5 Validation and Refinement of Algorithm:

Given target dimensions, the algorithm serves as a tool to determine starting dimensions that will anneal to the correct shape. Additionally, the algorithm is flexible because different combinations of layer thicknesses and raster angles can be used to achieve the same shape. To validate the algorithm, a goal final shape was first chosen. The algorithm was then utilized to produce four designs which had different initial dimensions and print parameters that would then deform into the same goal shape. Four samples of each design were printed, measured, and annealed. The average final post-annealed measurements of each design was compared to the pre-designed goal shape dimensions. A design was considered a success if the final dimension was within 5% of the pre-designed goal shape dimensions.

3. Results

3.1 Heat Transfer in Annealing Process

Initially, the samples were annealed in a small Jeio Tech vacuum oven directly on metal shelves. The resulting annealed samples showed significant warping off of the oven shelf in the direction of the Y-axis shown in the left sample in Figure 10, likely due to rapid heat transfer from the metal shelves. To avoid warping, later samples were annealed on McMaster-Carr firebricks, a material with low thermal conductivity and high thermal mass which allows for less rapid heat transfer and reduced temperature fluctuations when the oven door was opened. The reduced sample warping can be seen in the sample on the right in Figure 10 which made Z-axis strain easier to measure and helped produce more consistent results.

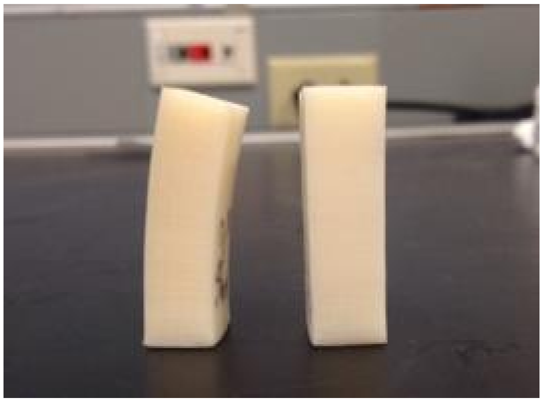

Figure 10: A sample annealed without a firebrick (left) and with a firebrick (right)

The first five sets of anneal time tests were done in the Jeio Tech vacuum oven. A separate oven was used for all other annealing, including reruns of 3 of the initial 5 anneal time tests. The second oven, a VWR small utility oven, was selected because of its small size. While both ovens had 1 cubic foot of internal volume, they had different temperature uniformity. The Jeio Tech had a more uniform temperature with fluctuations of ± 3.7°C compared to the VWR's ± 6.0°C [20,21]. Previous research from D’Amico et al., which this project builds upon, utilized the Jeio Tech vacuum oven for all of the annealing, to which we attribute a portion of the difference between the data sets [3]. This and other possible sources of variance, is discussed in section 3.5.

3.2 Effect of Gravity on Anneal Process

To determine whether gravity had an effect on the deformation of samples, 0°/100µm samples were annealed with the XZ-plane parallel to the oven base and compared to samples with the same build parameters that were annealed with the YZ-plane parallel to the oven base. The samples annealed with YZ-plane parallel to the oven base were marked as ‘Gravity’ and the XZ-plane parallel samples are marked as ‘Control’ in Figure 11 below. Samples with a raster angle of 0° typically showed strain in the X and Z-axes but little to none in the Y-axis. Since the XZ-plane was parallel to the oven for these samples, it was hypothesized that gravity may have been flattening the samples when they were above T_g. Multiple one-way analysis of variance (ANOVA) comparing the strain in the X-axis, Y-axis, and Z-axis directions between the gravity and control samples were carried out. A value of 0.05 was used for α (the probability of incorrectly rejecting the null hypothesis) and the null hypothesis was no difference between groups. The null hypothesis was not rejected for X-axis strain (p=.4784), Y-axis strain (p=.0513) and Z-axis strain (p=.7418). In Figure 11, no differences in strain were observed between the two annealing orientations. Y-axis strain was still very low in the gravity samples even though the YZ-plane was parallel to the base. These results demonstrated that the strain was not appreciably influenced by gravity. With this information, the effect of gravity was deemed to be negligible and the annealing protocol did not change. All subsequent samples were heated with the XZ-plane parallel to the oven base.

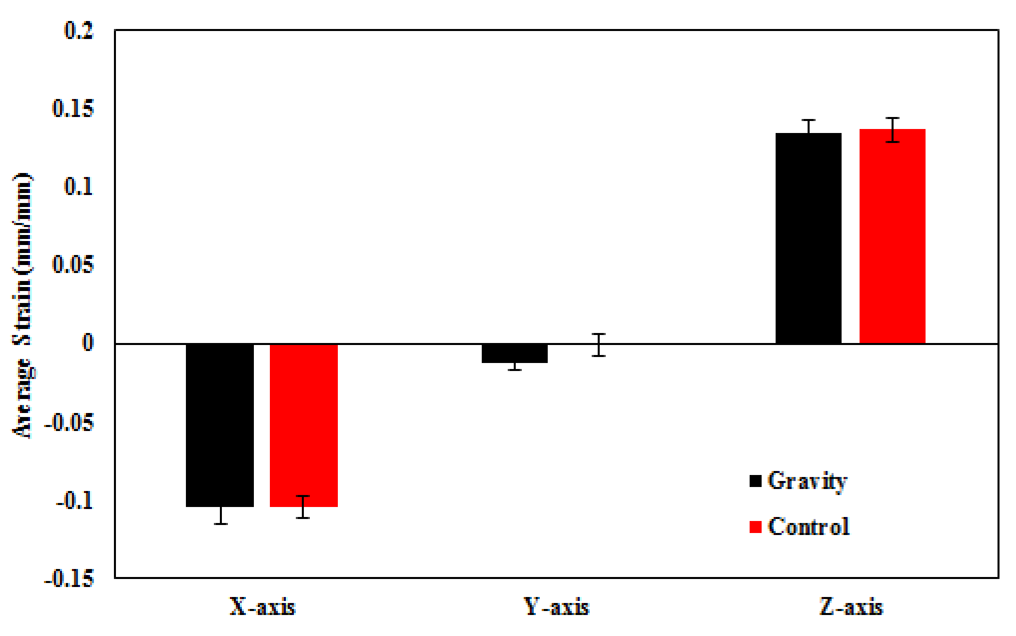

Figure 11: Gravity vs. Control Samples

3.3 Print Parameters

Samples were originally printed with 70% infill and extrusion width set to the auto value of 0.48mm. These samples had visible gaps between the extruded roads. Therefore, the infill percentage was increased until no visible voids were observed. Fewer voids were desired because air pockets could affect how the samples deformed during annealing. Void formation for various infill percentages is shown in the Figures 12 and 13. In Figures 12-13, the percentage of voids drastically decreased as the infill percentage increased. 100% infill was selected due to the complete lack of visible voids in the layers. The extrusion width was also changed and set to 0.45mm to match the actual measured width of extruded filament.

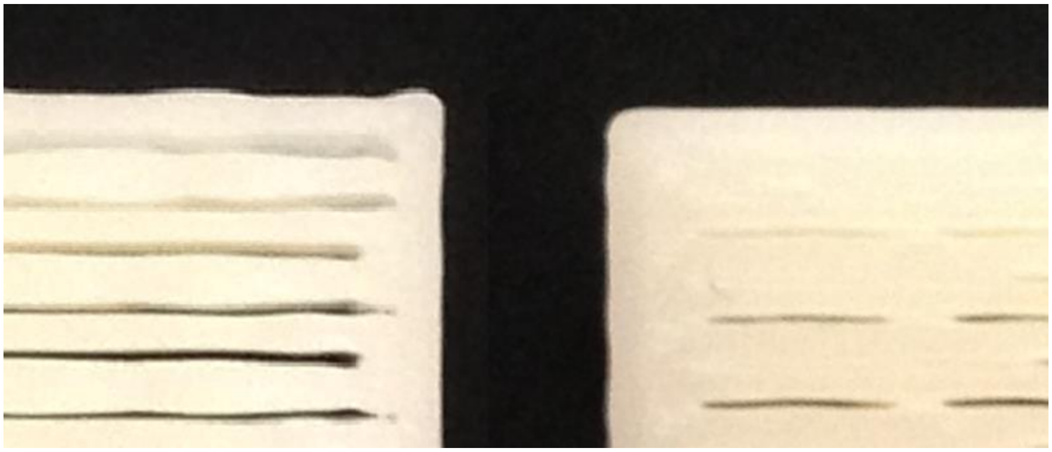

Figure 12: On the left, 70% infill. On the right, 80% infill

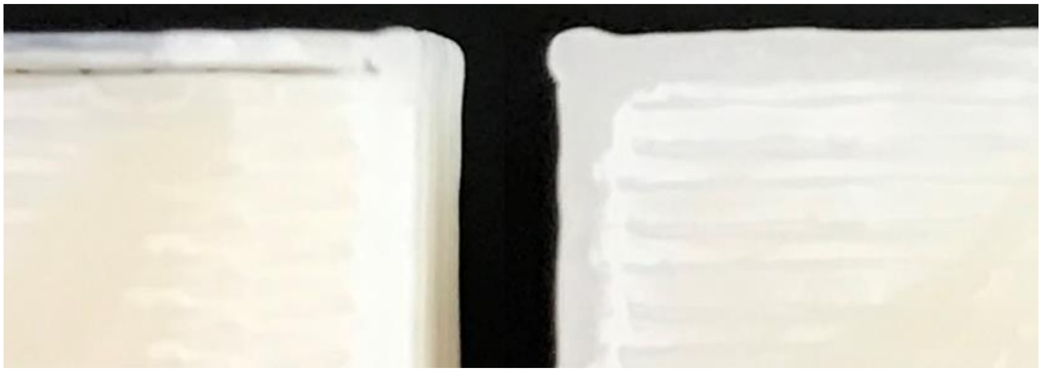

Figure 13: On the left, 90% infill and 100% infill on the right

3.4 Determine Optimal Annealing Time:

To minimize the annealing time of each sample while still achieving full expansion/contraction, 45 control samples at 100 µm layer thickness were printed in batches of 5. Samples were annealed for 5, 10, 15, 20, 25, 30, 35, 40, and 45 hours with 5 samples for each annealing duration. Additionally, samples were randomly assigned an anneal time to avoid error associated with inconsistencies in samples printed in different batches. Each sample was allowed to equilibrate at room temperature for one day. Samples were then measured in all axes. The amount of deformation in the X-axis, Y-axis, and Z-axis directions was plotted as a function of time to find the time at which the shape transformation did not vary a substantial amount from one anneal time to the next. After this time of annealing, the samples were assumed to have annealed fully. Figures 14-16 show the anneal time results for measurements in the X-axis, Y-axis, and Z-axis directions. An outlier was shown at the 30hr time point with large degrees of error. The reason for this outlier was not determined but time points after 30hrs were shown to have more consistent magnitudes of strain. Multiple one-way ANOVA comparing the strain in the X-axis, Y-axis, and Z-axis directions between samples annealed for 35, 40, and 45 hours was carried out. A value of 0.05 was used for α and the null hypothesis was no difference between groups. The null hypothesis was rejected for X-axis strain (p=.6911), Y-axis strain (p=.7433), and Z-axis strain (p=.9198).

Based on these results, the annealing time was taken as t_{anneal} = 48 hours to ensure that the samples were completely annealed.

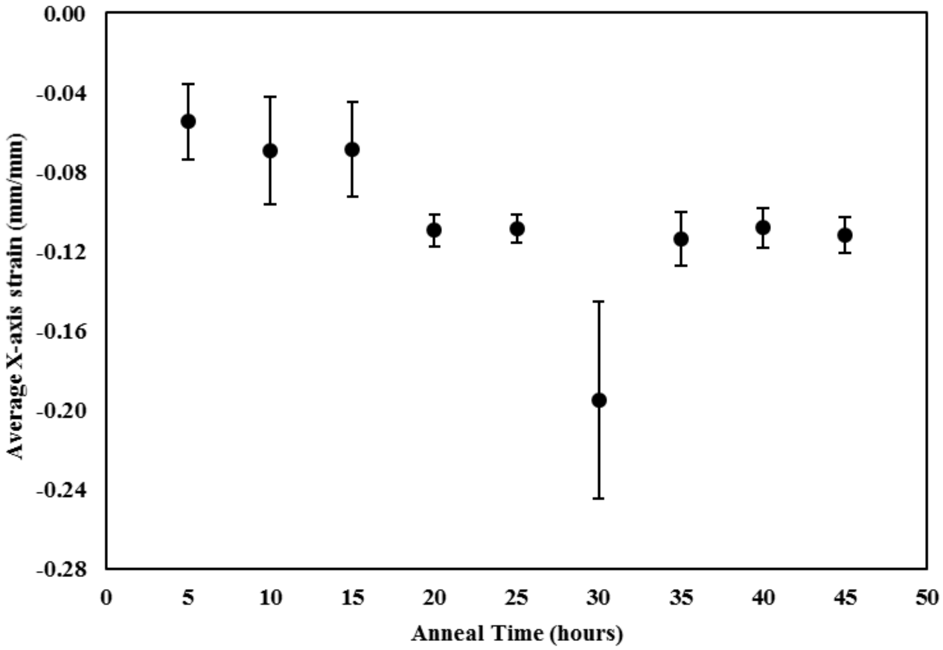

Figure 14: X-axis Strain vs. Anneal Time

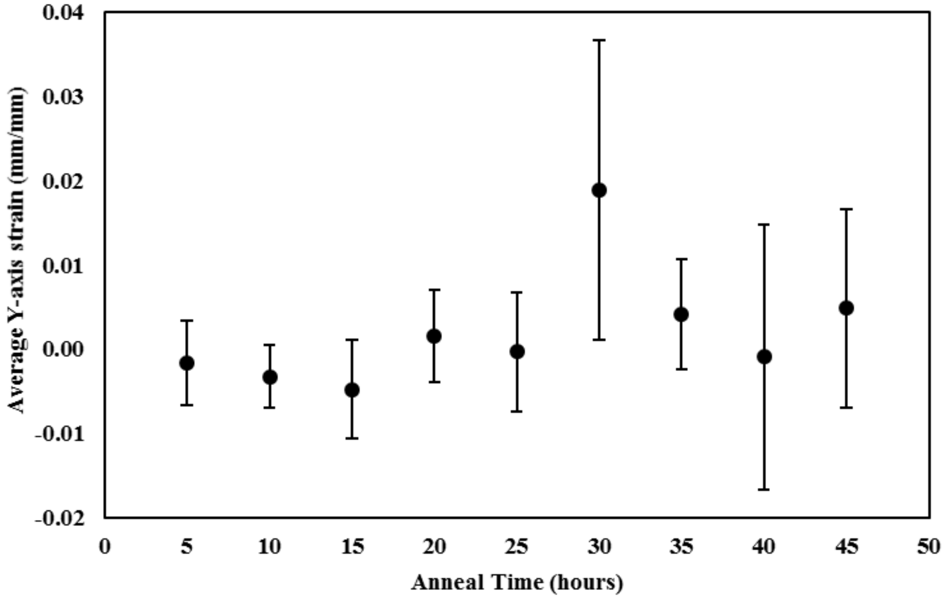

Figure 15: Y-axis Strain vs. Anneal Time

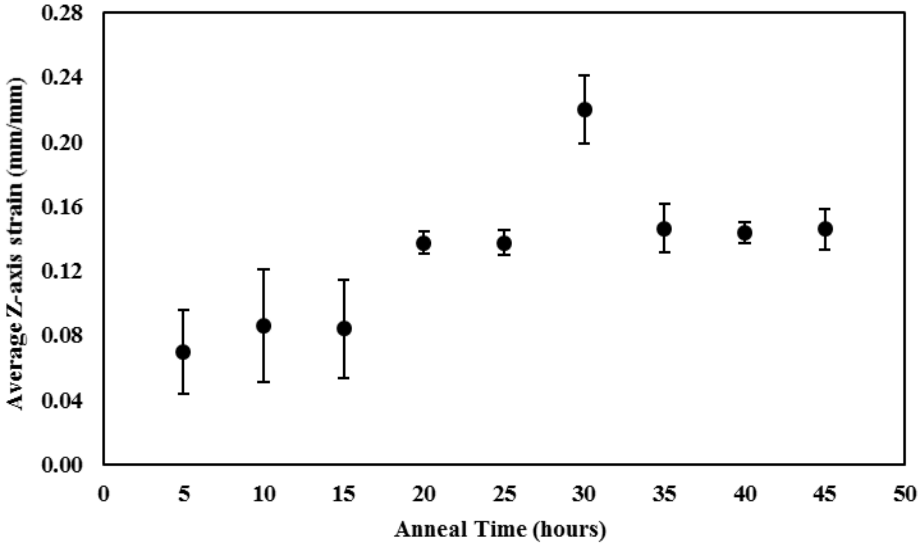

Figure 16: Z-axis Strain vs. Anneal Time

3.5 Effect of Layer Thickness

Figure 17 shows that increasing layer thickness results in lower magnitudes of irreversible thermal strain. Of the four layer thicknesses tested, the 100μm samples exhibited the greatest magnitude of strain.

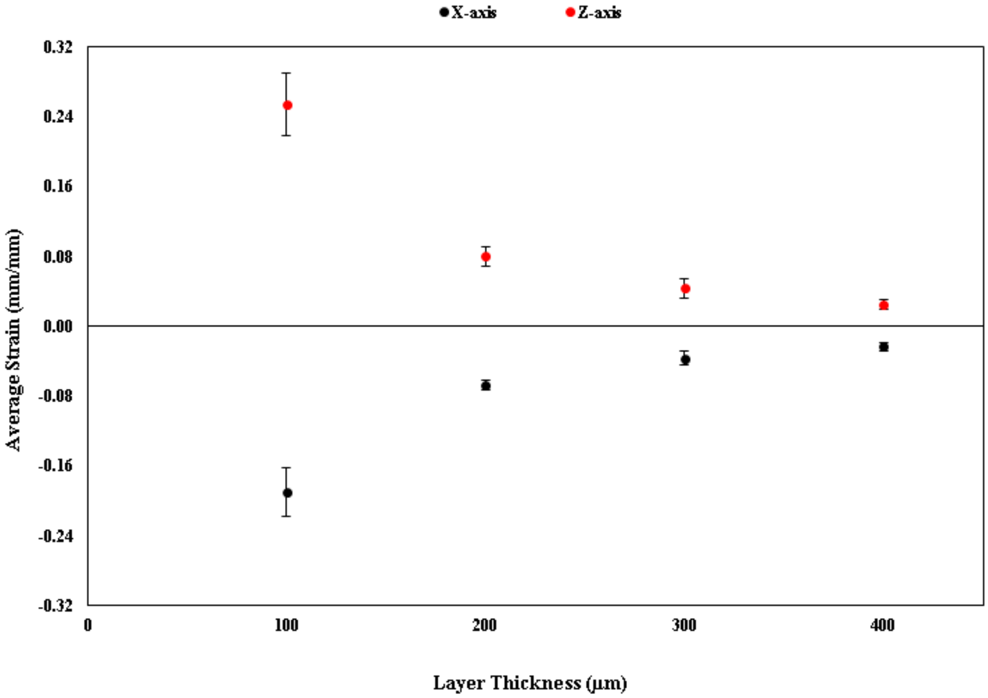

Figure 17: Average Strain vs. layer thickness for 0° degree raster in the X and Z-axis

Maximum strain is to be expected in the 100 µm samples because decreasing the layer thickness increases the number of roads and layers. While the trends seen in previous research and the data from this project are consistent, they do not have the same strain values as expected but instead vary by 1-3%. The difference was likely partially caused by the different temperature uniformities of the ovens used. Samples from the previous research also had different dimensions which could result in varied strains caused by different patterns of extrusion. However, even with these differences, the consistency in trends confirms that increasing layer thickness reduces the magnitude of irreversible strain.

3.6 Overall Effect of Raster Angle

The effects of raster angle on the resultant irreversible thermal strain has not been previously investigated in a systematic fashion. Prior research showed strain in the X-axis and Z-axis directions but little to none in the Y-axis [3]. The previous research used a Y-axis length of 2mm so the lack of measured Y-axis strain could be related to difficulty in taking accurate measurements of the small amounts of strain. To avoid this possible problem, a Y-axis length of 10mm was chosen for this research and the data gained confirms a strong relationship between the raster angle and the direction of strain (Figures 18, 19). Since the 100µm samples exhibited the most deformation, they also gave the clearest trends in the data. As seen in Figure 18, at 0°/100µm, the X-axis strain is near its maximum value of –20% while the Y-axis strain is near 0%. This relationship is flipped at 90° raster angle where the Y-axis experiences its greatest amount of deformation at about –18% strain and the X-axis has near 0% shown in Figure 19. Fitting the equations to the first principles is discussed in detail in the algorithm section.

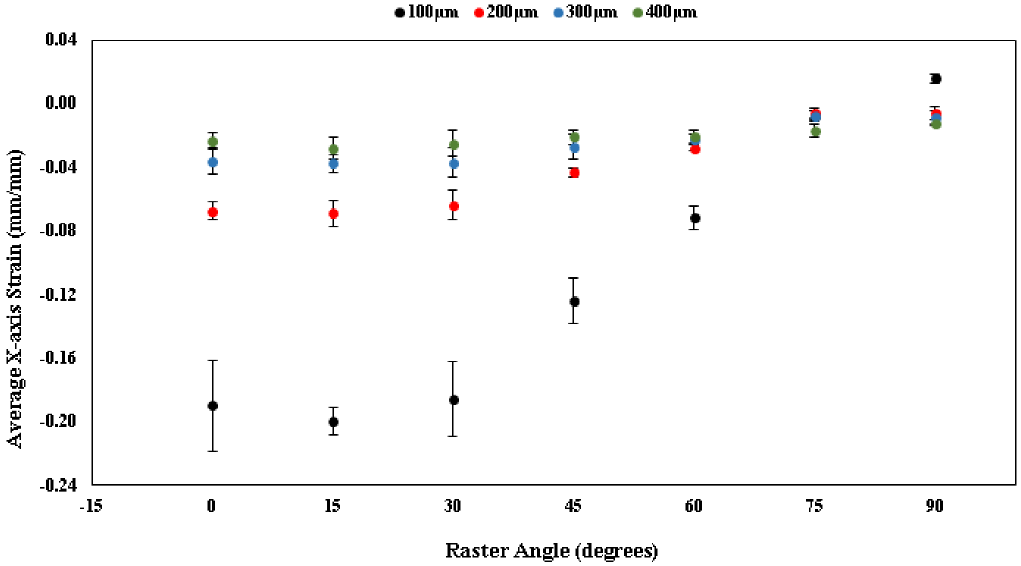

Figure 18: Average X-axis strain vs. raster angle

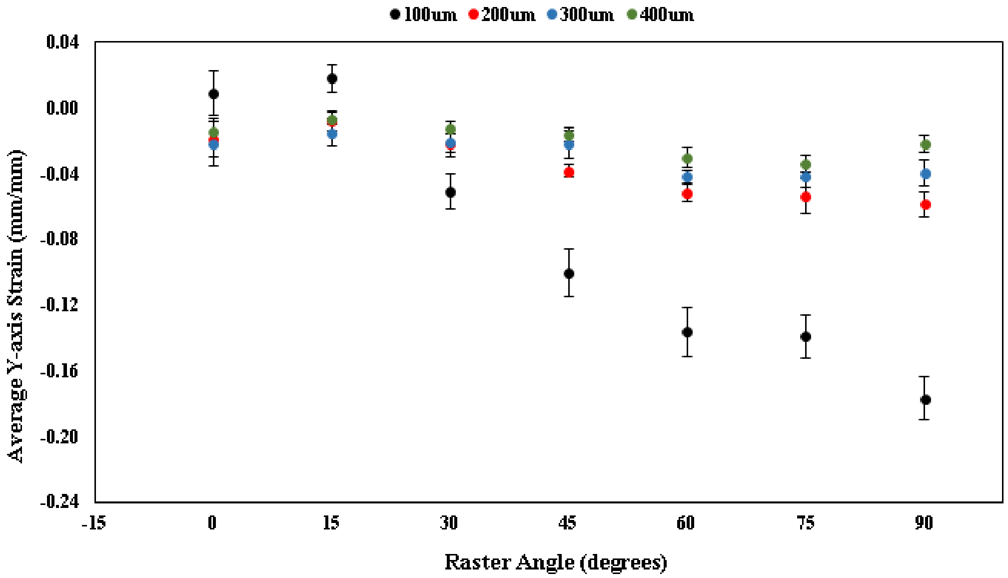

Figure 19: Average X-axis strain vs. raster angle

The general trends for X-axis and Y-axis are that, as raster angle increases, the X-axis strain decreases in magnitude while the Y-axis strain increases, as seen in Figures 18 and 19, respectively. The trend of increased magnitude of strain with decreasing layer thickness is again observed with the trend holding over all raster angles.

The Z-axis is slightly more complex, with no clear trend in the data as a function of raster angle (Figure 20). One-way ANOVA was performed for Z-axis strain at each layer thickness. In each case, the null hypothesis was rejected at a confidence interval of 95% ($p < 0.05$), indicating that there are statistically significant differences in strain as a function of raster angle. However, the theory predicts no influence from raster angle on Z-axis strain. This suggests that something other than raster angle may be affecting the Z-axis strain.

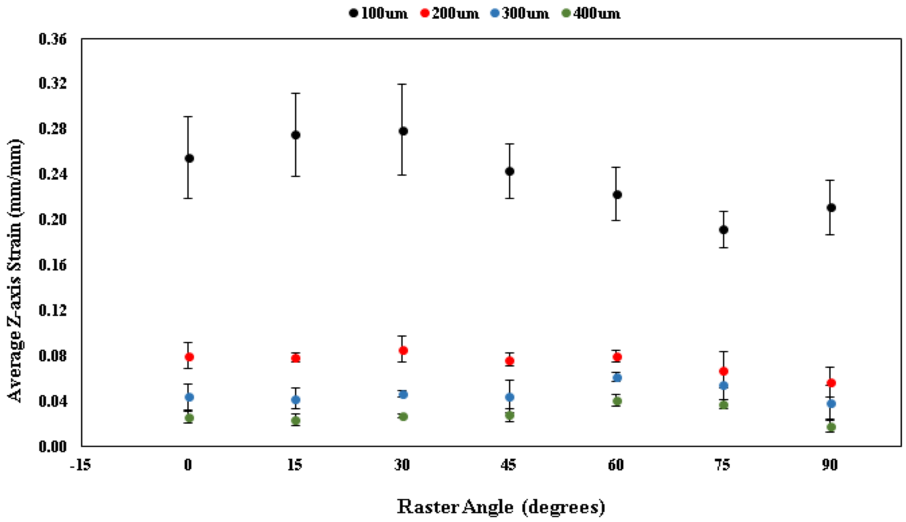

Figure 20: Average Z-axis strain vs. raster angle

As stated previously, stress is imparted in the direction of the roads [3]. Therefore, samples are expected to contract in the direction of the raster angle. The stress down the roads is gradually pointed away from the X-axis and into the Y-axis as raster angle is increased. Therefore, the negative strain in the Y-axis is gradually increased while X-strain approaches zero as seen in the data. These trends are observed in the theoretical equations discussed in section 3.7.

Shown in Figure 21, as the raster angle increases, the shear strain increases from 0° to a maximum of about 15° in the 100µm samples, which occurs at the 30° and 45° raster angles. The shear strain then falls back to about 0° as raster angle approaches 90°. The derived equation for shear strain accurately predicts a maximum shear strain at 45° as well as the lack of shear strain at 0° and 90° as discussed in the following section. Again, the magnitude of strain, in this case, shear strain, is shown to decrease with increasing layer thickness.

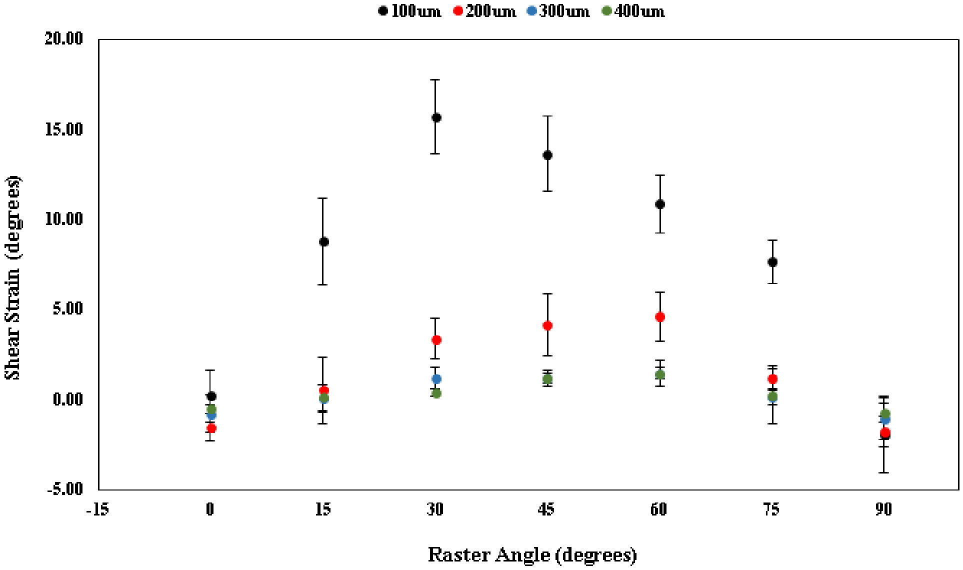

Figure 21: Shear strain vs. raster angle at various layer thicknesses

3.7 Discussion of Algorithm

The algorithm was composed of the four equations for ε_x, ε_y, ε_z, and γ_{xy}. The derivation for these equations can be found in section 2.4 and are shown below as Equations 24-27.

$$\varepsilon_x = \frac{F_r}{E * w_r * l_t} * (cos^2(\Theta) - v_{xy} sin^2(\Theta)) \qquad \textbf{\textit{(Eq. 24)}}$$

$$\varepsilon_y = \frac{F_r}{E * w_r * l_t} * (sin^2(\Theta) - v_{xy} cos^2(\Theta)) \qquad \textbf{\textit{(Eq. 25)}}$$

$$\varepsilon_z = \frac{F_r}{E * w_r * l_t} * (-v_z) \qquad \textbf{\textit{(Eq. 26)}}$$

$$\gamma_{xy} = \frac{F_r}{E * w_r * l_t} * sin(\Theta) * cos(\Theta) * 2(1 + v_{xy}) \qquad \textbf{\textit{(Eq. 27)}}$$

A non-linear least squares fit, via the Solver plug-in in Excel, was used to fit Equations 24-27 to the recoded data. $\frac{F_r}{E}$, v_{xy}, and v_z were used as fitting variable in the equations. $\frac{F_r}{E}$ was determined to be -0.0079, v_{xy} was -0.035, and v_z was 5.95. The Poisson ratio is defined as the negative ratio of the change in strain in one axis divided by the change in strain in another. Therefore, a negative near 0 value for v_{xy} makes sense due to negative strain in both axes and strains at 0° and 90° raster angles primarily occurring in one direction. Additionally, a positive value for v_z makes sense due to the positive values of strain occurring in the Z-axis and negative values of strains in both the X and Y-axis directions.

The non-linear least squares fit for Equation 24 to the measured X-axis strain is shown in Figure 23. Table 1 shows which color on Figures 22-25 correspond to which layer thickness. Error bars on Figures 22-25 represent a 95% confidence interval.

Layer Thickness
100µm
200µm
300µm
400µm

Table 1: Color and Corresponding Layer Thickness

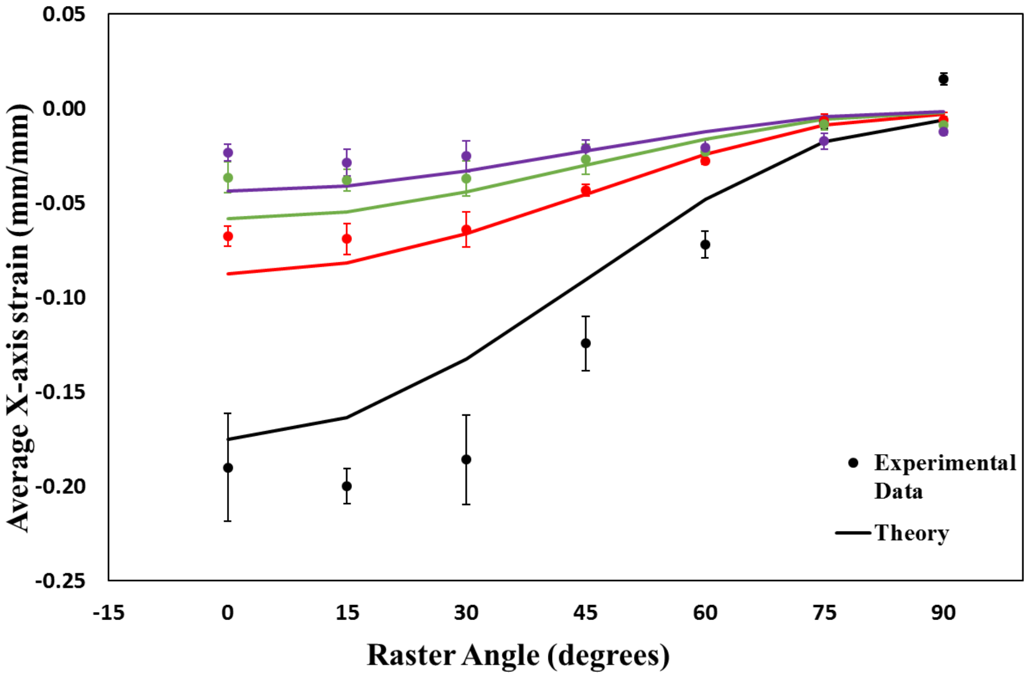

Figure 22: Calculated X-axis Strain vs. Measured Strain at 100µm-400µm

In Figure 22, 0.956, 0.970, 0.919, and 0.787 are the R^2 values for the X-axis strain at 100µm, 200µm, 300µm, and 400µm respectively. As the layer thickness increased, a decrease in the R^2 was observed. This may be due to the difficulty in measuring small amounts of strain exhibited at higher layer thicknesses. Additionally, the uncertainty of all X-axis strain measurements was 0.004. While insignificant in measurements of large magnitudes of strain, this uncertainty limits the ability to measure the small amounts of strain that occur at higher layer thicknesses. Therefore, to discern more accurate trends in the strain of larger layer thicknesses, a more accurate measurement tool is recommended. In Figure 22, maximum X-axis strain was exhibited at a raster angle of 0° and a minimum at 90°. This agrees with the theory that the raster force only acts parallel to the extruded roads. Therefore when roads are parallel to the X-axis, the raster force is only acting in the X-axis direction and causes the observed maximum X-axis strain. In contrast, when roads are perpendicular to the X-axis a minimum or near 0 value for strain is expected. Figure 23 represent the fit of Equation 25 to the measured Y-axis strain data.

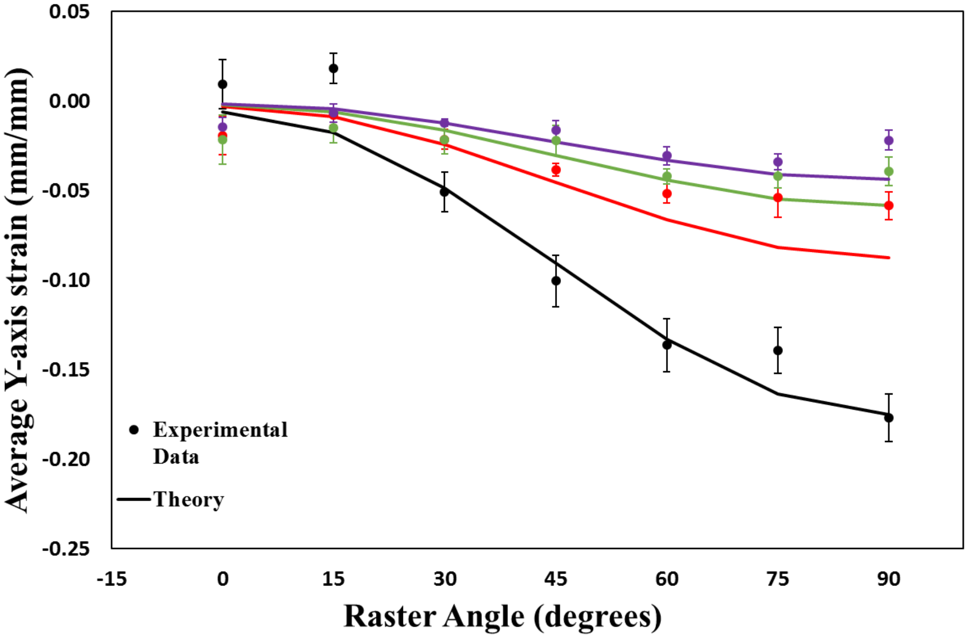

Figure 23: Calculated Y-axis Strain vs. Measured Strain at 100µm-400µm

In Figure 23, 0.955, 0.939, 0.826, and 0.680 are the R^2 values for Y-axis strain at 100µm, 200µm, 300µm, and 400µm respectively. This may be due to the same reasons given for the X-axis strain above. An uncertainty of nearly all Y-axis strain measurements was calculated as 0.006. Additionally, a minimum Y-axis strain at 0° raster angle and maximum Y-axis strain at 90° was observed. This agrees with the theory that the raster force only acts parallel to the extruded roads. Thus when the roads are parallel with the Y-axis, raster angle of 90°, a maximum is observed. And when the roads are perpendicular with the Y-axis, raster angle of 0°, a minimum is observed. The trend between layer thickness and R^2 was not seen in the fit of Equation 26 to Z-axis strain data. An R^2 value of 0 was calculated for all Z-axis strain fits, due the theory not predicting any correlation between Z-axis strain and raster angle. Thus, knowing the raster angle does not help predict Z-axis strain based on the theoretical equation. The fit of Equation 26 to Z-axis strain data is shown in Figure 24.

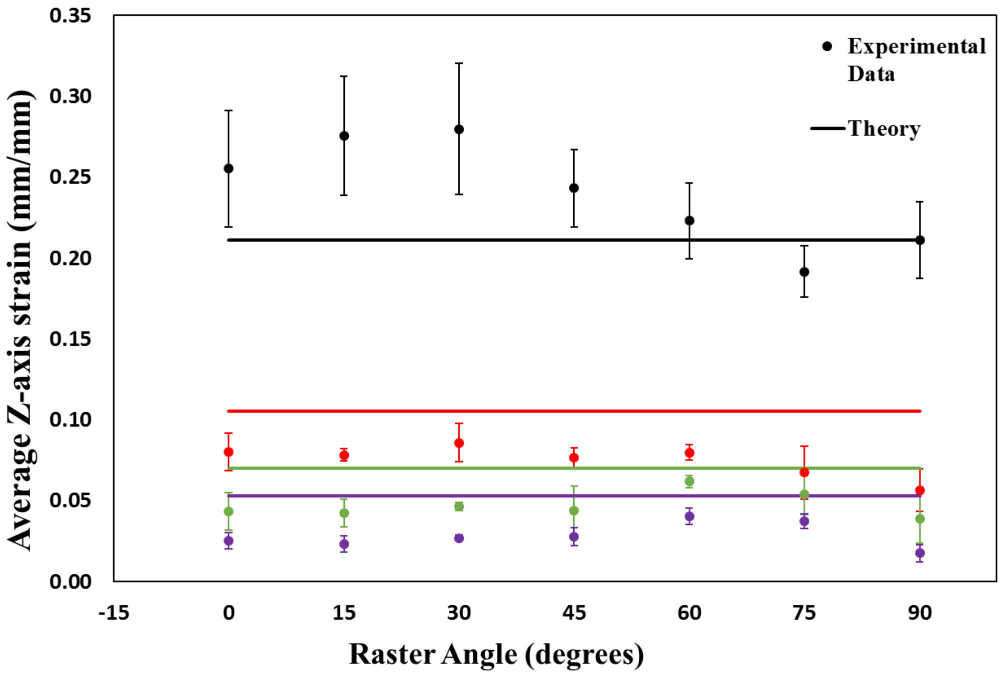

Figure 24: Calculated Z-axis Strain vs. Measured Strain at 100µm-400µm

In the Z-axis strain data the calculated values of strain form a straight line due Z-axis strain not being dependent on raster angle. One-way ANOVA comparing the average Z-axis strain over all raster angles was performed for each layer thickness. A value of 0.05 was used for α and the null hypothesis was no difference between groups. Surprisingly, the null hypothesis was rejected for Z-axis strain at 100µm (p=0.0077), 200µm (p=0.0259), and 400µm (p=9.58E-05) but was not rejected at 300µm (p=0.129). This contradiction between the ANOVA of each layer thickness in the Z-axis strain data suggests a correlation does exist and further research needs to be done between Z-axis strain and raster angle. Additionally, the calculated uncertainty for all Z-axis strain measurements was 0.002. The Z-axis strain decreased as layer thickness increased. This agrees with the layer thickness being inversely proportional to the raster stress, given by Equation 28.

$$\sigma_{raster} = \frac{F_r}{E*w_r*l_t} \qquad \textbf{\textit{(Eq. 28)}}$$

As raster stress decreases the exhibited Z-axis strain decreases. Lastly, Figure 25 shows the fit of Equation 27 to the measured shear strain data.

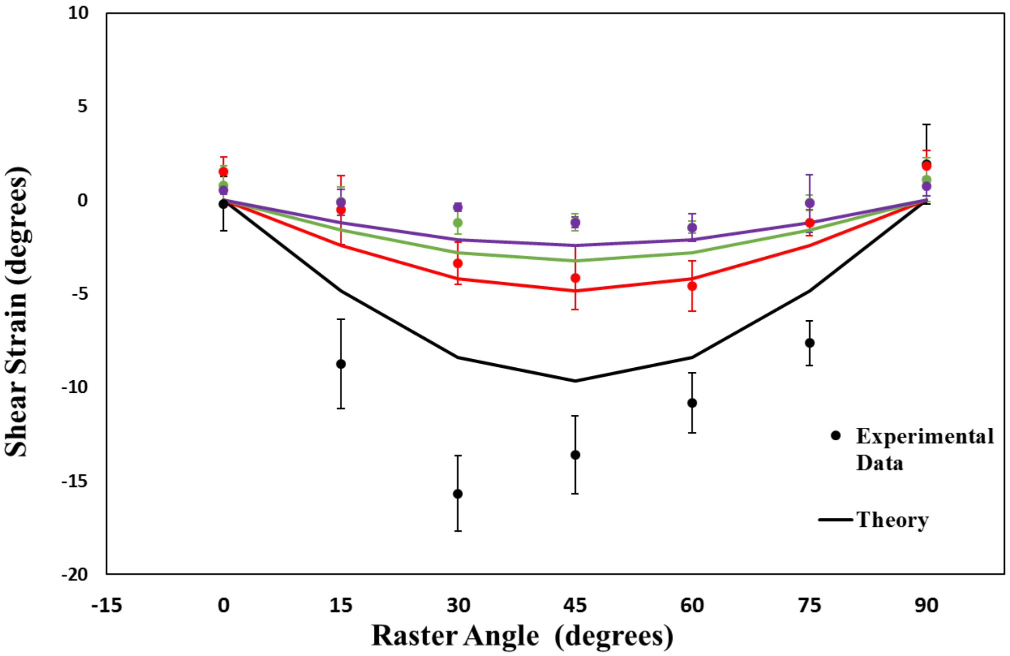

Figure 25: Calculated Shear Strain vs. Measured Shear Strain at 100µm-400µm

Similarly to the trend seen in the X and Y-axis strain data, the R^2 value for shear strain also decreases as layer thickness increases. The values for R^2 were 0.927, 0.956, 0.955, and 0.841 at 100µm, 200µm, 300µm, and 400µm respectively. This may be due to the reasons stated for X and Y-axis strain. Additionally, an uncertainty was unable to be calculated due to the method of measuring raster angle. A maximum value of shear strain was exhibited at a raster angle of 30° and no shear strain was exhibited at 0° and 90° raster angles. This agrees with the theory because when the raster force is only acting in the X-axis (0° raster angle) or Y-axis (90° raster angle) no shear strain is expected because the raster force is only acting in one direction. Additionally, at raster angles between 30° and 60° maximum shear strain is expected because the raster force is acting in both the X and Y-axis directions. A maximum shear strain is experienced when the X and Y components of the raster force are equal.

3.8 Proof of Concept

A final shape with the given final dimensions was chosen. L_X is length in the X-axis direction, L_Y is the length in the Y-axis direction, L_Z is the length in the Z-axis direction, and γ_{xy} is the shear strain in the XY-plane.

$L_x = 20mm$

$L_Y = 20mm$

$L_Z = 20mm$

$\gamma_{xy} = 5°$

Using Equations 24-27 four designs were created with the following dimensions and print parameters. Refer to Table 2 for dimensions and build parameters of all design concepts.

Design	X-axis length (mm)	Y-axis length (mm)	Z-axis length (mm)	Raster angle (deg)	Layer thickness (mm)
1	23.0	20.4	11.2	19	0.10
2	22.3	20.5	12.2	24	0.12
3	21.7	20.6	13.0	30	0.14
4	21.1	20.9	13.6	41	0.16

Table 2: Initial dimensions of designs and print parameters

4 samples of each design were printed, annealed, and measured with the same process as described in the methodology. The percent error for the X-axis, Y-axis, and Z-axis is shown below in Figure 26. The shear strain for all design concepts are in Figure 27.

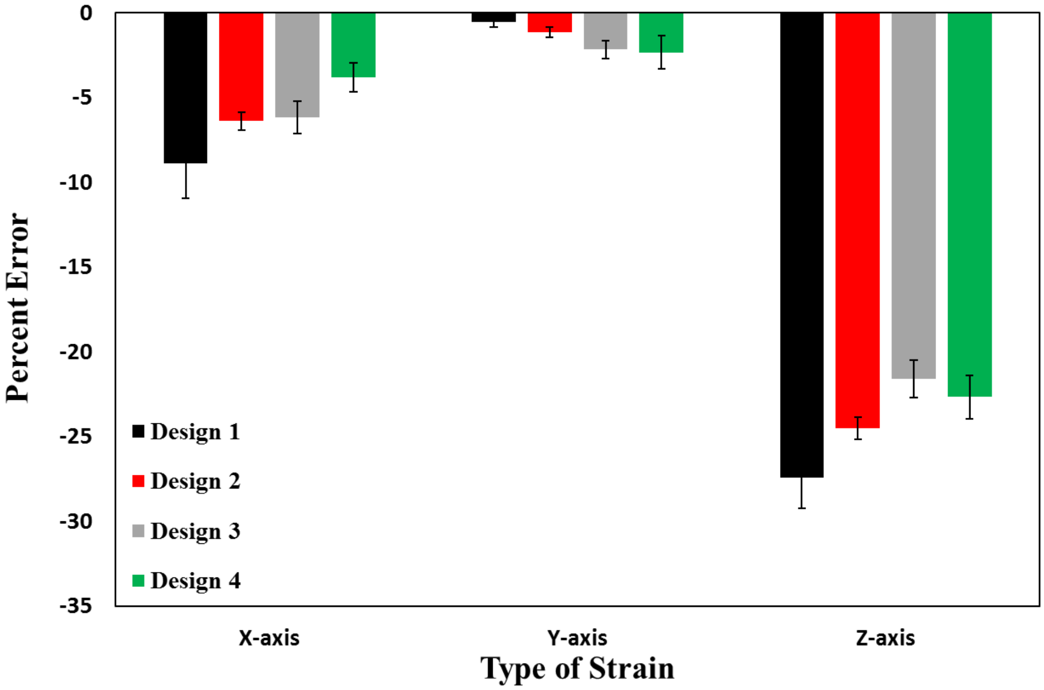

Figure 26: Percent Error vs. Type of Strain for all designs

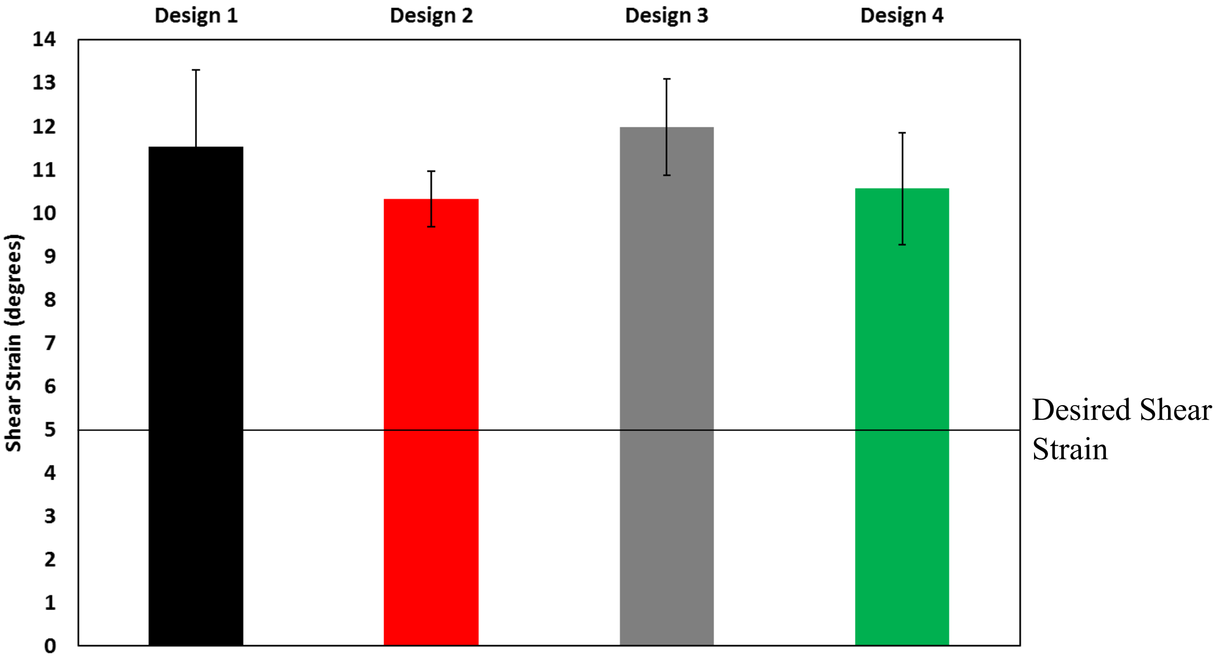

Figure 27: Shear Strain Deviation

Every design's Y-axis measurements were within 5% of the desired Y-axis dimension. Only the X-axis dimension of design 4 was within 5% of the desired X-axis dimension. All Z-axis dimensions of the design were not within 5% of the desired Z-axis dimension. This is likely due to the error in the fit of the theoretical Z-axis strain equation to experimental data. The shear strain was much less accurate than the other measurements. Each set of set of designs had an average shear strain of over 10° with a percent error over 100%. While the percent error is high, since the angles were only about 5° off in each case, the error is not very significant. Some of this error is caused by the inaccuracies in the theoretical equations for lower layer thicknesses. However, the large amount of error suggests that more research is necessary to accurately be able to determine the shear strain at lower layer thicknesses.

4. Conclusion

The work in this project sought to develop a relationship between irreversible thermal strain and the raster angle and layer thickness of FDM printed parts. Maximum strain in the X-axis direction was observed at raster angle of 0°. Maximum Y-axis strain was observed at raster angles of 90°. This supported the overarching theory that a raster force is acting parallel to the extruded roads. Additionally, the overall magnitude of strain showed an inversely proportional relationship to layer thickness. This supports the theory that as layer thickness increases the raster stress decreases due to fewer layers. The algorithm created within this project predicts strain well in certain axes and needs further development in others. X and Y-axis strain can be accurately predicted at this point given layer thickness and raster angle. Data for Z-axis strain does not match the predicted trend in the derivation of Hooke's Law. Lastly, the shear strain prediction is inaccurate at smaller layer thicknesses. While the trend of the data follows that of the theoretical curve, the data does not fall along the line. This suggests that some influence on the shear strain was not captured in the theoretical equation. The proof of concept completed showed that the strain could be predicted to a degree. Again, X and Y-axis strain were predicted well while accurate Z-axis and shear strain predictions were not achieved.

Additional research is needed in exploring, Z-axis strain, shear strain, raster width of samples, and raster outline surrounding the infill of the part to achieve a greater understanding of the residual stresses within FDM printed parts. However, this project is a crucial first step in relating theory to observed irreversible thermal strain in AM. With a slightly modified, more accurate set of equations, the research of this project could be used in a wide range of FDM printing applications. The development of a prediction method for strain would greatly help with producing strong FDM printed parts with reduced residual stresses and having parts anneal into the correct shape.

References

[1] S.H. Huang, P. Liu, A. Mokasdar, L. Hou, Additive manufacturing and its societal impact: a literature review 67 (2013) 1191-1203.

[2] E. Palermo, Fused Deposition Modeling: The Most Common 3D Printing Method. http://www.livescience.com/39810-fused-deposition-modeling.html, 2013.

[3] A. D'Amico, A. Debaie, Peterson M. Amy, Effect of layer thickness on irreversible thermal expansion and interlayer strength in fused deposition modeling (2013).

[4] A. Kantaros, D. Karalekas, Fiber Bragg grating based investigation of residual strains in ABS parts fabricated by fused deposition modeling process, Mater Des 50 (2013) 44-50.

[5] A. Lindstrom, Selective Laser Sintering, Birth of an Industry. http://www.me.utexas.edu/news/news/selective-laser-sintering-birth-of-an-industry, 2012.

[6] 3D Matter, What is the influence of infill %, layer height and infill pattern on my 3D prints?. http://my3dmatter.com/influence-infill-layer-height-pattern/, 2015.

[7] W. Wu, P. Geng, G. Li, D. Zhao, H. Zhang, J. Zhao, Influence of layer thickness and raster angle on the mechanical properties of 3D-printed PEEK and a comparative mechanical study between PEEK and ABS 8 (2015) 5834-5846.

[8] What are the main 3D Printing Parameters?. http://3dprinting-blog.com/tag/3d-printing-parameters/, 2014 (accessed Feb 14, 2017).

[9] W. Hipolite, Number of Shells (2015).

[10] T. Wang, J. Xi, Y. Jin, A model research for prototype warp deformation in the FDM process 33 (2007) 1087-1096.

[11] S. Wang, A.G. Miranda, C. Shih, A study of investment casting with plastic patterns, Mater. Manuf. Process. 25 (2010) 1482-1488.

[12] J. Hu, Shape Memory Polymers, 1. publ. ed., Smithers Rapra, Shrewsbury, 2014.

[13] M. Behl, A. Lendlein, Shape-memory polymers, Springer, Berlin [u.a.], 2010.

[14] C. Liang, C.A. Rogers, E. Malafeew, Investigation of Shape Memory Polymers and Their Hybrid Composites 8 (1997) 380-386.

[15] J.A. Hiltz, Shape Memory Polymers (2002).

[16] A.K. Bhowmick, Mechanical Properties of Polymers 1 (2002).

[17] Wikipedia, A schematic representation of the shape-memory effect (2009).

[18] D. Dean, Differential Scanning Calorimetry (2014).

[19] Szymon Wojtyła, Piotr Klama, Tomasz Baran, Is 3D printing safe? Analysis of the thermal treatment of thermoplastics: ABS, PLA, PET, and nylon (2017) 0.

[20] Jeio Tech Co., Inc. OV-11-120 Vacuum Oven. https://www.hogentogler.com/jeio-tech/ov-11-120-vacuum-oven.asp, 2017.

[21] VWR International. VWR Constant Temperature Ovens. http://www.americaninstrument.com/pdf/3691F-OVEN.pdf